

## PDF hosted at the Radboud Repository of the Radboud University Nijmegen

The following full text is a postprint version which may differ from the publisher's version.

For additional information about this publication click this link.

<http://hdl.handle.net/2066/109250>

Please be advised that this information was generated on 2017-12-06 and may be subject to change.

**Title:**

Quantitative Assessment of Heterogeneity in Tumor Metabolism using FDG-PET

**Running title:**

FDG Metabolic Heterogeneity in Tumors

**Authors:**

\* Dennis Vriens, MD

\* Jonathan A. Disselhorst, MSc

Wim J.G. Oyen, MD, PhD

Lioe-Fee de Geus-Oei, MD, PhD

Eric. P. Visser, PhD

*\* Both authors contributed equally*

**Affiliation:**

Department of Nuclear Medicine

Radboud University Nijmegen Medical Centre

Nijmegen, The Netherlands

**Correspondence:**

D. Vriens

Radboud University Nijmegen Medical Centre, Department of Nuclear Medicine 444

Geert Grooteplein-Zuid 8, 6525 GA Nijmegen, The Netherlands

Tel: +31-24-3614048; Fax: +31-24-3618942; E-mail: [d.vriens@nucmed.umcn.nl](mailto:d.vriens@nucmed.umcn.nl)

## **Conflicts of Interest:**

Siemens Molecular Imaging kindly provided the software for the analyses. Otherwise there are no financial or other relationships that could be construed as a conflict of interest.

## Abstract

**Purpose:** [ $^{18}\text{F}$ ]-fluorodeoxyglucose-positron emission tomography (FDG-PET) images are usually quantitatively analyzed in "whole-tumor" volumes of interest. Also parameters determined with dynamic PET acquisitions, such as the Patlak glucose metabolic rate ( $\text{MR}_{\text{glc}}$ ) and pharmacokinetic rate constants of 2-tissue compartment modeling are most often derived per lesion. We propose segmentation of tumors to determine tumor heterogeneity, potentially useful for dose-painting in radiotherapy and elucidating mechanisms of FDG uptake.

**Methods and Materials:** In 41 patients with 104 lesions dynamic FDG PET was performed. On  $\text{MR}_{\text{glc}}$  images, tumors were segmented in quartiles of background subtracted maximum  $\text{MR}_{\text{glc}}$  (0 – 25%, 25 – 50%, 50 – 75% and 75 – 100%). Pharmacokinetic analysis was performed using an irreversible two-tissue compartment model in the three segments with highest  $\text{MR}_{\text{glc}}$  to determine the rate constants of FDG-metabolism.

**Results:** From the highest to the lowest quartile, significant decreases of uptake ( $K_1$ ), washout ( $k_2$ ) and phosphorylation ( $k_3$ ) rate constants were seen with significant increases in tissue blood volume fraction ( $V_b$ ).

**Conclusions:** Tumor-regions with highest  $\text{MR}_{\text{glc}}$  are characterized by high cellular uptake and phosphorylation rate constants with relatively low blood volume fractions. In regions with less metabolic activity, the blood volume fraction increases and cellular uptake, washout and phosphorylation rate constants decrease. These results support the hypothesis that regional tumor glucose phosphorylation rate is not dependent on the transport of nutrients (i.e., FDG) to the tumor.

## Keywords

Fluorodeoxyglucose F18 – Positron-Emission Tomography – Pharmacokinetics –  
Tissue Distribution – Patlak analysis

## Introduction

Positron emission tomography (PET) is a molecular imaging technique to quantitatively assess various tissue properties with an appropriate radiotracer such as [ $^{18}\text{F}$ ]-fluoromisonidazole (FMISO) for hypoxia [1] or [ $^{18}\text{F}$ ]-fluorothymidine (FLT) for proliferation [2]. However, [ $^{18}\text{F}$ ]-fluorodeoxyglucose (FDG), which visualizes glucose metabolic processes in tissues, remains the most commonly used radiotracer with PET. FDG-PET has obtained a clear role in tumor staging [3] and is used to assess therapy response and predict outcome [4]. In most cases the standardized uptake value (SUV) is used to quantify whole-tumor FDG-uptake. Most tumors however, display heterogeneous uptake in FDG-PET images, which may reflect different biologic behavior in the different regions within these lesion. Identifying this metabolic heterogeneity would not only be useful for understanding tumor biology, but might be of prognostic significance or of use for radiotherapy planning and dose painting by intensity-modulated radiation therapy (IMRT) as well [5].

To examine processes underlying the uptake of FDG in a tumor, sophisticated quantification methods such as determination of pharmacokinetic rate constants of 2-tissue compartment models can be used [6;7], requiring dynamic PET images. With these pharmacokinetic analyses, the properties of the FDG metabolism can be elucidated. Delivery of FDG in and out the cell corresponds to the rate constants  $K_1$  and  $k_2$ , respectively. Once intracellular, phosphorylation of FDG is represented by  $k_3$ , dephosphorylation by  $k_4$ , and  $V_b$  finally, indicates the fraction of blood within the volume of interest (VOI). The 2-tissue compartment model of FDG metabolism is shown in figure 1. Pharmacokinetic rate constants, and other model-based parameters are usually derived in a VOI, mostly representing the whole tumor. These parameters therefore, correspond to averaged values of tumor glucose metabolic activity. To assess intratumoral heterogeneity, the parameters could be obtained for every individual voxel within the tumor (voxel-wise modeling). The time-activity curves for single voxels, however, are relatively noisy. This prevents accurate determination of tumor parameters using non-linear least squares (NLLS) methods [8]. Moreover, tumor movement (e.g., as a result of breathing) has a relatively large influence in these small volumes as in this case each voxel does not necessarily represent a single volume of tissue.

As a trade-off, less detailed parameters (such as the metabolic rate of glucose ( $\text{MR}_{\text{glc}}$ )) can be used, for which voxel-wise quantification is feasible, since they can be based on linearization methods

which are far less sensitive to noise (e.g., using the Patlak method [9]). Another method to overcome high noise levels is to decrease spatial image resolution by reconstruction at smaller matrix sizes. Post-reconstruction smoothing could also be used to increase signal-to-noise ratios at the cost of spatial resolution.

Similarly, higher signal-to-noise ratios can be obtained by tumor segmentation and taking the mean value in each segment, which could be used to determine tumor regional variation in 2-tissue compartment model rate constants of FDG metabolism ( $K_1-k_4$ ) and blood volume fraction ( $V_b$ ).

We applied the latter method and segmented the tumors based on the  $MR_{glc}$  images, taking advantage of the higher tumor-to-background ratio as compared to standard uptake images [10]. Furthermore, we wanted to verify our hypothesis that tumor regions with the highest  $MR_{glc}$  are characterized by high FDG extraction and phosphorylation rates.

## Patients & methods

### 1. Patient population & data acquisition procedure

From an existing database of dynamic FDG-PET scans of oncological patients acquired on a Siemens ECAT EXACT47 (Siemens Healthcare), 41 patients with 104 tumors of different origin (table 1) were selected [11; 12]. Selection criteria were: previously untreated patients in whom a fully arterially sampled input function is available. The study was approved by the Institutional Review Board of the Radboud University Nijmegen Medical Centre and written informed consent was obtained from each patient. Details of the study have been described before with the only difference that the present images were reconstructed in  $128 \times 128 \times 47$  matrices using 2D ordered subsets expectation maximization (OSEM2D) with 4 iterations and 16 subsets and a 5 mm 3-dimensional (3D) Gaussian filter. In brief, fasted patients were injected with FDG by an automated standardized infusion protocol. Immediately thereafter, 17 arterial blood samples were taken at set time points from which plasma was obtained to provide a sampled arterial plasma time activity concentration curve ( $C_{plasma}(t)$ ). Simultaneously, a dynamic PET-acquisition consisting of 16 time-frames of variable duration was obtained to provide the tissue time activity curve). Voxel volumes in the reconstructed images were  $39.75 \text{ mm}^3$  (transaxial voxel size  $3.432 \times 3.432 \text{ mm}$ , axial voxel size  $3.375 \text{ mm}$ ).

## 2. Data analysis

Data analysis was performed using Inveon Research Workplace (IRW version 2.2, Siemens Healthcare). First, voxel-wise Patlak linear regression [9] of acquired data 10 – 50 min post injection (the last 5 time-frames) was used to obtain the influx constant ( $K_i$ ) of each voxel. The slope of the Patlak plot equals  $K_i$ , and  $MR_{glc}$  was calculated by multiplication with the measured venous plasma glucose concentration, thereby assuming a lumped constant (LC) of 1, see equation 1. The real value of LC is time and tissue dependent and therefore unknown [13].

$$MR_{glc} = \frac{[Glc]}{LC} K_i = \frac{[Glc]}{LC} \frac{K_1 k_3}{k_2 + k_3} \quad (1)$$

Since pharmacokinetic analysis of dynamic data is sensitive to time-delay ( $t_d$ , i.e., the difference in time of arrival of the FDG-bolus in the tumor and in the sampled artery), manual time-offset synchronization of  $C_{plasma}(t)$  and  $C_{tumor}(t)$  of  $VOI_{tumor}$  was performed by visually shifting the ascending limbs of both curves until they overlapped.

On images of  $MR_{glc}$ , one representative background VOI ( $VOI_{BG}$ ) and three tumor VOIs were determined per lesion, defined by increasing levels of background-corrected  $MR_{glc}$  ( $VOI_{low}$ ,  $VOI_{medium}$  and  $VOI_{high}$ , summing up to  $VOI_{tumor}$ ; table 2). The quartile with lowest metabolic rate was not included, as the edges of the metabolic volume may contain non-tumor tissues and the noise levels in this segment is higher due to a lower FDG uptake. We did not attempt any partial-volume correction strategies.  $VOI_{BG}$  was defined as an ellipsoidal volume of at least the size of the corresponding tumor and placed in a representative volume of tissue with normal FDG-uptake (e.g., contralateral lung in case of a lung metastasis).

IRW uses the iterative Levenberg-Marquardt algorithm for NLLS curve fitting, minimizing the weighted least squares deviation [14] to obtain all rate constants and  $V_b$  simultaneously, in each tumor VOI separately. The weighting function was chosen as the square root of the frame duration divided by the measured non-decay-corrected activity concentration in each time frame (i.e., Poisson weighting). For initialization of the NLLS algorithm, multiple (=99), randomly selected starting parameters within a defined range (0.0 – 2.0 for the rate constants, 0.0 – 1.0 for  $V_b$ ) were used.

Data from the literature suggest that the rate of dephosphorylation of FDG by glucose-6-phosphatase activity ( $k_4$  in the Phelps 4K [7]) is very low in mammalian tissues, except in liver tissue [15]. Moreover, from simulation studies it has been warned that a  $k_4$  might result from tissue

heterogeneity rather than real dephosphorylation [16]. All pharmacokinetic analyses were performed using the Sokoloff 3K ( $K_1$ - $k_3$ ) model [6], as it showed a better fit than the Phelps 4K ( $K_1$ - $k_4$ ) model [7] in a majority of lesions (data on file).

The resulting values for each parameter were classified as being biologically plausible or not. Values within 3 standard deviations (99.7% confidence interval) of the mean described elsewhere [17; 18] were considered biologically plausible by definition. This criterion was set to label unrealistic tumor parameter values, which could be the result of the instability of the nonlinear optimization of extremely noisy time-activity concentration curves. For  $K_1$  this meant the interval  $0 - 1.049 \text{ mL}\cdot\text{g}^{-1}\cdot\text{min}^{-1}$ , for  $k_2$   $0 - 1.455 \text{ min}^{-1}$ , for  $k_3$   $0 - 0.511 \text{ min}^{-1}$  and for  $V_b$   $0.001 - 0.335$ . The subgroup of lesions considered having biologically plausible results was analyzed separately, to validate that the conclusions drawn based on the whole group were not due to (implausible) outliers. Next, in order to evaluate the influence of blurring caused by the partial-volume effect and motion, the subgroup of lesions with a volume of at least  $14.1 \text{ cm}^3$  were analyzed, as this volume represents a lesion with a spherical diameter of  $\sim 3 \text{ cm}$ , which is 5 times the resolution of the scanner ( $\sim 0.6 \text{ cm}$  full width at half maximum).

Finally, these parameters were interpreted in view of their reliability (relative standard error) and mutual independence (correlation matrix).

### 3. Statistical analysis

(Log<sub>e</sub>)-normally distributed variables are described by mean and 95%-confidence interval (95%-CI: mean  $\pm 1.96 \times$  standard deviation). Variables not obeying the (log<sub>e</sub>)-normal distribution are described by median and interquartile range (IQR). For normally distributed values the (paired) t-test and the squared Pearson's Product-Moment Correlation Coefficient ( $R^2$ ) were used to compare means or express correlation. In case of non-normality, Spearman's  $\rho$  was used. Correlation was qualified based on  $R^2$ : very high ( $R^2 \geq 0.9$ ), high ( $0.7 < R^2 < 0.9$ ), intermediate ( $0.5 < R^2 < 0.7$ ) or low ( $R^2 < 0.5$ ).

Comparison of multiple groups was performed by non-parametric analysis of variance (Friedman's ANOVA). To correct for multiple comparisons, a *post-hoc* analysis with Wilcoxon signed rank test was conducted with a Dunn's (or Bonferroni's) correction.



Relations between tumor parameters on the one hand and biological plausibility on the other hand were determined using univariable logistic regression. The following continuous variables were candidate predictors: volume,  $K_1$ ,  $MR_{glc}$  and SUV of the smallest VOI (segment). Their discriminative ability was evaluated by determination of the area under the receiver operating characteristics curves (AUC). Difference between the AUC and 0.500 (i.e., AUC for an indiscriminate test) was assessed by asymptotic distribution assumption for significance. All statistical analyses were performed using SPSS version 16.0.2. The cut-off point for statistical significance was set at 0.05.

## Results

Median lesion volume based on  $VOI_{tumor}$  was  $11.3 \text{ cm}^3$  (corresponding to 283.5 voxels), ranging from  $1.7$  to  $504 \text{ cm}^3$  (42 to 12668 voxels). VOI characteristics of tumor segments are displayed in *table 3*.

Correlation of the  $VOI_{tumor}$  parameters showed significant but weak correlation between  $MR_{glc}$  and  $K_1$  ( $\rho: 0.286$ ,  $p=0.003$ ),  $MR_{glc}$  and  $k_3$  ( $\rho: 0.488$ ,  $p < 0.001$ ) but not between  $MR_{glc}$  and  $k_2$  ( $\rho: -0.088$ ,  $p = 0.372$ ) and  $MR_{glc}$  and  $V_b$  ( $\rho: 0.189$ ,  $p = 0.055$ ). There was also no significant correlation between  $k_3$  and  $V_b$  ( $\rho: 0.045$ ,  $p = 0.652$ ). The subgroup of NSCLC showed similar results, as summarized in *table 4*.

An example of lesion segmentation with corresponding time-activity concentration curves is displayed in *figure 2*. As demonstrated in *figure 3*, a clear trend in reduction of  $K_1$ ,  $k_2$ ,  $k_3$  and increase in  $V_b$  was observed from  $VOI_{high}$  toward  $VOI_{low}$ , which was significant for all four investigated parameters. The within-group differences were significant between all segments, except for  $VOI_{high}$  versus  $VOI_{medium}$  for both  $K_1$  and  $k_2$ . These trends were seen in significantly more than the expected 25% (if divided equally between the 4 possibilities) of the analyzed lesions: 42% (95%-CI: 33 – 52%) for  $K_1$ , 40% (95%-CI: 31 – 50%) for  $k_2$ , 79% (95%-CI: 70 – 86%) for  $k_3$  and 93% (95%-CI: 87 – 97%) for  $V_b$ . Similar trends are observed when NSCLC and CRC lesions are considered separately. Forty lesions had a volume larger than  $14.1 \text{ cm}^3$ . In this subgroup, the trends were observed in a higher percentage of the lesions, as displayed in *table 5*.

In 90% of the lesions all four  $VOI_{tumor}$  parameters were considered biologically plausible. In the 10 lesions with one or more implausible parameters,  $K_1$  was not within the defined plausible range in

20%,  $k_2$  in 70%,  $k_3$  in 40% and  $V_b$  in 50% of these lesions. Multivariable logistic regression showed only  $K_1$  to be independently related to plausibility.

When looking at the four parameters in the segments  $VOI_{high}$ ,  $VOI_{medium}$  and  $VOI_{low}$  separately, in 45 lesions (43% of the analyzed tumors) all 12 values were within the range of biologic plausibility. In the other 59 lesions (57%) with at least one or more resulting implausible parameters in one or more VOIs,  $K_1$  was not within the plausible range in 15%,  $k_2$  in 81%,  $k_3$  in 34% and  $V_b$  in 61% of these lesion. Only the smallest  $K_i$  was related to biologically plausible results, which had moderate discriminative ability (AUC 0.680, 95%-CI: 0.578 – 0.783).

When looking only at the 45 lesions with all 12 values within the defined range of biological plausibility we saw similar trends between  $VOI_{high} - VOI_{low}$  for  $K_1$ ,  $k_3$  and  $V_b$ . However this did not reach statistical significance for  $k_2$  (Friedman = 2.80,  $p = 0.257$ , downslope trend for  $VOI_{high} - VOI_{low}$  in 33%), see table 5.

For the 312 NLLS operations (3 tumor segment VOIs in each of the 104 lesions), 10% of  $K_1$ , 10% of  $k_2$ , 12% of  $k_3$  and 20% of  $V_b$  showed relative standard errors larger than 5%. In the 104 (larger VOI) whole-tumor parameters this was only the case in 4%, 4%, 5% and 5% respectively. Correlation matrices of the 312 parameters, showed very high mutual dependence between  $K_1$  and  $k_2$  (median R: 0.96, IQR: 0.96 – 0.97), intermediate mutual dependence between  $K_1$  and  $V_b$  (median R: -0.73, IQR: -0.83 – -0.68) and low mutual dependence between  $K_1$  and  $k_3$  (median R: 0.06, IQR: -0.38 – 0.43), between  $k_2$  and  $k_3$  (median R: 0.36, IQR: -0.13 – 0.68), between  $k_2$  and  $V_b$  (median R: -0.60, IQR: -0.70 – -0.54) and between  $k_3$  and  $V_b$  (median R: 0.34, IQR: 0.03 – 0.66).

## Discussion

When comparing tumor regions with stepwise decreasing  $MR_{glc}$ , there is decreasing phosphorylation rate ( $k_3$ ) but increasing fractional blood volume ( $V_b$ ). This cannot be explained by mutual dependence of these variables in the fitting process, since the fit-correlation was low. We could not find a significant correlation between whole-tumor  $V_b$  and  $k_3$  between lesions. Glucose phosphorylation rate therefore is not correlated with lesion blood volume fraction. Miles and Williams [19] have reviewed the relation between tumor vascularization and tumor metabolism. Although the total uptake of FDG is considered rather than  $k_3$ , they show that literature on this subject is highly

variable. It was reported that the relationship appeared to depend on tumor type, tumor size and tumor grade. In this study, even in the subgroups per tumor type or the subgroup of large tumors there were no significant correlations between  $V_b$  and  $k_3$ , see table 4. The weak correlations between  $MR_{glc}$  and  $k_3$  (significant) and  $MR_{glc}$  and  $V_b$  (not significant) might indicate that using  $MR_{glc}$  as tumor segmentation variable is responsible for the within-patient inverse relation between the  $k_3$ - and  $V_b$ -trends over the segments, but the absence of between-lesion correlation between  $V_b$  and  $k_3$  suggests another underlying mechanism. Multiple groups reported a correlation between FDG-uptake during the first few minutes after injection and tumor blood-flow measured by [ $^{15}O$ ]-H<sub>2</sub>O in various tumor types [20;21]. Since a large  $V_b$  is mainly responsible for the tumor FDG-concentration in the (very) early time-frames, at which blood FDG activity concentrations are still very high, our results suggest that  $V_b$  (hence regional tumor perfusion) is inversely related with phosphorylation rate ( $k_3$ ). Our results suggest that the “metabolic center” of the tumor can maintain high phosphorylation rates ( $k_3$ ) at relatively low blood volume fractions ( $V_b$ ). This interesting result may support the hypothesis that as the tumor grows, angiogenesis becomes unable to maintain an adequate blood supply, contributing to the uncoupling of glucose metabolism and blood flow, a theory also known as the Warburg Effect [22]. It should be noted that  $V_b$  as obtained with pharmacokinetic modeling may not reflect the complete blood fraction in the tumor. The venous blood time activity curve may have a shape very different from the arterial blood time activity curve as used for the compartment analysis. This could result in an underestimation of  $V_b$ .

Tumor hypoxia is disadvantageous property for several cancer treatments including radiation therapy [23]. Numerous methods to detect or visualize hypoxia in vivo are available which include hypoxia specific PET tracers such as FMISO. Some suggest to employ FDG-PET for dose painting because of the disadvantages of hypoxia tracers, e.g., a low tumor to background ratio, low reproducibility, and slow clearance of these tracers in non-hypoxic regions [24]. Although FDG is certainly not a tracer specific for hypoxia, there is a correlation between FDG uptake and hypoxia in tumors [25]. More details about the metabolism of FDG can be obtained using dynamic PET. We have shown an inverse relation between  $V_b$  and  $k_3$ , which might be indicative for a poorer oxygenation in the metabolic centre of the tumor, because of increased demand of oxygen and nutrients (higher phosphorylation), but decreased delivery (lower volume fraction of blood). Continuous uptake of FDG, despite a poor vasculature, is a sign of adaptation of the

tumor to the hypoxic conditions. The intratumoral metabolic heterogeneity suggests differences in the tumor microenvironment (including distribution of hypoxia), which might have an impact on radiation treatment planning.

We do not believe that the high number of lesions with outlying parameters influenced our conclusions as we saw similar results in the subgroup of lesions in which all parameter values were considered biologically plausible.

A potentially disturbing factor is image blurring, both due to partial-volume-effects and (periodic) movements such as breathing. However, the subgroups of lesions least influenced by both causes of blurring (i.e., tumor volumes at least 5 times the scanners spatial resolution) showed similar results to the whole-group analysis, which demonstrates the limited role of these perturbing factors on our results.

## Conclusion

Regions of tumors with highest  $MR_{glc}$  are characterized by high cellular uptake and phosphorylation rate constants with relatively low blood volume fractions. In regions with less metabolic activity, the blood volume fraction gradually increases and cellular uptake, washout and phosphorylation rate constants decrease. These results are not due to covariance of the regression coefficients and might be relevant for understanding tumor biology and for dose-painting in radiotherapy.

## Acknowledgement

We would like to thank Siemens Molecular Imaging for providing the software, and specifically X.B. Pan and J. Declerck for commenting on the manuscript.

## References

1. Rajendran J, Krohn K. PET Imaging for Tumor Hypoxia: Characterizing the Tumor and Guiding Treatment. In: Valk PE et al., eds. *Positron Emission Tomography*. London: Springer; 2006:359-374.

2. Barwick T, Bencherif B, Mountz JM, *et al.* Molecular PET and PET/CT imaging of tumour cell proliferation using F-18 fluoro-L-thymidine: a comprehensive evaluation. *Nucl Med Commun.* 2009;30:908-17.
3. Hillner BE, Siegel BA, Liu D, *et al.* Impact of positron emission tomography/computed tomography and positron emission tomography (PET) alone on expected management of patients with cancer: initial results from the National Oncologic PET Registry. *J Clin Oncol.* 2008;26:2155-61.
4. Geus-Oei L-F de, Vriens D, Laarhoven HWM van, *et al.* Monitoring and predicting response to therapy with 18F-FDG PET in colorectal cancer: a systematic review. *J Nucl Med.* 2009;50 Suppl 1:43S-54S.
5. Ford EC, Herman J, Yorke E, *et al.* 18F-FDG PET/CT for image-guided and intensity-modulated radiotherapy. *J Nucl Med.* 2009;50:1655-65.
6. Sokoloff L, Reivich M, Kennedy C, *et al.* The [14C]deoxyglucose method for the measurement of local cerebral glucose utilization: theory, procedure, and normal values in the conscious and anesthetized albino rat. *J Neurochem.* 1977;28:897-916.
7. Phelps ME, Huang SC, Hoffman EJ, *et al.* Tomographic measurement of local cerebral glucose metabolic rate in humans with (F-18)2-fluoro-2-deoxy-D-glucose: validation of method. *Ann Neurol.* 1979;6:371-88.
8. Hong YT, Fryer TD. Kinetic modelling using basis functions derived from two-tissue compartmental models with a plasma input function: general principle and application to [18F]fluorodeoxyglucose positron emission tomography. *Neuroimage.* 2010;51:164-72.
9. Patlak CS, Blasberg RG, Fenstermacher JD. Graphical evaluation of blood-to-brain transfer constants from multiple-time uptake data. *J Cereb Blood Flow Metab.* 1983;3:1-7.
10. Visser EP, Philippens MEP, Kienhorst L, *et al.* Comparison of tumor volumes derived from glucose metabolic rate maps and SUV maps in dynamic 18F-FDG PET. *J Nucl Med.* 2008;49:892-8.
11. Geus-Oei L-F de, Der Heijden HFM van, Visser EP, *et al.* Chemotherapy response evaluation with 18F-FDG PET in patients with non-small cell lung cancer. *J Nucl Med.* 2007;48:1592-8.
12. Geus-Oei L-F de, Laarhoven HWM van, Visser EP, *et al.* Chemotherapy response evaluation with FDG-PET in patients with colorectal cancer. *Ann Oncol.* 2008;19:348-52.
13. Wienhard K. Measurement of glucose consumption using [(18)F]fluorodeoxyglucose. *Methods.* 2002;27:218-25.
14. Moré JJ. The Levenberg-Marquardt algorithm: Implementation and theory. In: Watson GA, ed. *Lect Notes Math.* Vol 630. 630th ed. Berlin: Springer; 1978:105-116.
15. Okazumi S, Isono K, Enomoto K, *et al.* Evaluation of liver tumors using fluorine-18-fluorodeoxyglucose PET: characterization of tumor and assessment of effect of treatment. *J Nucl Med.* 1992;33:333-9.
16. Schmidt K, Lucignani G, Moresco RM, *et al.* Errors introduced by tissue heterogeneity in estimation of local cerebral glucose utilization with current kinetic models of the [18F]fluorodeoxyglucose method. *J Cereb Blood Flow Metab.* 1992;12:823-34.
17. Strauss LG, Klippel S, Pan L, *et al.* Assessment of quantitative FDG PET data in primary colorectal tumours: which parameters are important with respect to tumour detection? *Eur J Nucl Med Mol Imaging.* 2007;34:868-77.
18. Liu P, Huang G, Dong S, *et al.* Kinetic analysis of experimental rabbit tumour and inflammation model with 18F-FDG PET/CT. *Nuklearmedizin.* 2009;48:153-8.
19. Miles KA and Williams RE. Warburg revisited: imaging tumour blood flow and metabolism. *Cancer Imaging* 2008;8:81-86.

20. Mullani NA, Herbst RS, O'Neil RG, *et al.* Tumor blood flow measured by PET dynamic imaging of first-pass 18F-FDG uptake: a comparison with 15O-labeled water-measured blood flow. *J Nucl Med.* 2008;49:517-23.
21. Hoekstra CJ, Stroobants SG, Hoekstra OS, *et al.* Measurement of perfusion in stage IIIA-N2 non-small cell lung cancer using H(2)(15)O and positron emission tomography. *Clin Cancer Res.* 2002;8:2109-15.
22. Warburg O. On the origin of cancer cells. *Science.* 1956;123:309-14.
23. Höckel M, Vaupel P. Tumor hypoxia: definitions and current clinical, biologic, and molecular aspects. *J Natl Cancer Inst.* 2001;93:266-76.
24. Aerts HJWL, Lambin P, Ruyscher DD. FDG for dose painting: a rational choice. *Radiother Oncol.* 2010;97:163-4.
25. Rajendran JG. Hypoxia and Glucose Metabolism in Malignant Tumors: Evaluation by [18F]Fluoromisonidazole and [18F]Fluorodeoxyglucose Positron Emission Tomography Imaging. *Clin Cancer Res.* 2004;10:2245-2252.

## Figure legends

**Figure 1:** The 2-tissue compartment FDG model with pharmacokinetic rate constants  $K_1$ ,  $k_2$ ,  $k_3$ , and  $k_4$ . The measured PET signal (shown as a gray box) is a combination of FDG in tissue and a fraction of blood,  $V_b$ . The influx constant,  $K_i$ , can be calculated from the other rate constants with:  $K_1 k_3 / (k_2 + k_3)$ .

**Figure 2:** Representative example of a patient with cT<sub>3</sub>N<sub>2</sub>M<sub>0</sub> NSCLC. The lesion's largest diameter was 58 mm. **A:** a surface rendered image of the 3 VOIs clearly demonstrating the heterogeneity in FDG metabolism. **B:** the same lesion "opened up". **C:** graph showing the activity concentration curves in the 4 tumor VOIs (VOI<sub>low</sub>, VOI<sub>medium</sub>, VOI<sub>high</sub> and VOI<sub>tumor</sub>, left axis) and in the sampled arterial plasma (plasma, right axis). In **A** and **B**, the edge of VOI<sub>high</sub> is indicated with an arrowhead, and the edge of VOI<sub>medium</sub> with an arrow.

C<sub>plasma</sub>: sampled arterial plasma activity concentration, C<sub>tumor</sub>: tumor (VOI) activity concentration, NSCLC: non-small cell lung carcinoma, VOI: volume of interest.

**Figure 3:** Differences in rate constants and blood volume fraction in different tumor VOIs.

Friedman: Friedman's non-parametric analysis of variance overall test. NS: not significant, \*: significant with Wilcoxon signed rank test *post-hoc* analysis with Dunn's correction applied ( $p < 0.001$ ). VOI: volume of interest.

**Table 1:** Patient characteristics (n=41).

	Value	Range
Mean age [y]	60.8	44.7 – 77.7
Proportion male [%]	68.3	
Median plasma glucose level [mmol·L <sup>-1</sup> ]	5.2	4.2 – 8.3
Median AA per unit body mass [MBq·kg <sup>-1</sup> ]	2.7	1.6 – 5.9
Origin of primary tumor [% of patients]:		
NSCLC	71	
CRC	24	
Breast carcinoma	5	
Origin of primary tumor [% of lesions]:		
NSCLC	82	
CRC	16	
Breast carcinoma	2	
Proposed treatment [%]:		
Induction chemotherapy	22	
First line curative chemotherapy	76	
Palliative care	2	
Differentiation [%]:		
Poor	20	
Slight	15	
Moderate	27	
Mucinous	2	
Unknown	37	

AA: administered activity, CRC: colorectal carcinoma, NSCLC: non-small cell lung carcinoma.

**Table 2:** VOI definitions.

Name:	Lower bound:	Upper bound:
VOI <sub>high</sub>	$BG_{\text{mean}} + 0.75 (T_{\text{max}} - BG_{\text{mean}})$	$T_{\text{max}}$
VOI <sub>medium</sub>	$BG_{\text{mean}} + 0.50 (T_{\text{max}} - BG_{\text{mean}})$	$BG_{\text{mean}} + 0.75 (T_{\text{max}} - BG_{\text{mean}})$
VOI <sub>low</sub>	$BG_{\text{mean}} + 0.25 (T_{\text{max}} - BG_{\text{mean}})$	$BG_{\text{mean}} + 0.50 (T_{\text{max}} - BG_{\text{mean}})$
VOI <sub>tumor</sub>	$BG_{\text{mean}} + 0.25 (T_{\text{max}} - BG_{\text{mean}})$	$T_{\text{max}}$

$BG_{\text{mean}}$ : mean background  $MR_{\text{glc}}$ ,  $T_{\text{max}}$ : maximum tumor  $MR_{\text{glc}}$ .  $MR_{\text{glc}}$ : glucose metabolic rate. VOI: volume of interest.



**Table 3:** VOI characteristics.

	VOI <sub>tumor</sub>	VOI <sub>high</sub>	VOI <sub>medium</sub>	VOI <sub>low</sub>
Median Volume * [cm <sup>3</sup> ] (range)	11.3 (1.67 – 504)	0.556 (0.0795 – 8.11)	1.83 (0.278 – 92.2)	7.85 (1.07 – 406)
Mean MR <sub>glc</sub> † [nmol·mL <sup>-1</sup> ·min <sup>-1</sup> ] (95%-CI)	99.7 (36.4 – 274)	187 (69.8 – 503)	135 (50.3 – 361)	82.7 (30.9 – 221)
Median SUV [g·cm <sup>-3</sup> ] (IQR)	4.1 (2.8 – 5.5)	6.8 (4.8 – 8.7)	5.3 (3.7 – 6.8)	3.6 (2.5 – 4.8)
Median K <sub>1</sub> [mL·g <sup>-1</sup> ·min <sup>-1</sup> ] (IQR)	0.11 (0.077 – 0.16)	0.18 (0.81 – 0.37)	0.15 (0.092 – 0.23)	0.11 (0.072 – 0.15)
Median k <sub>2</sub> [min <sup>-1</sup> ] (IQR)	0.44 (0.25 – 0.89)	0.99 (0.31 – 2.9)	0.55 (0.29 – 1.1)	0.40 (0.22 – 0.75)
Median k <sub>3</sub> [min <sup>-1</sup> ] (IQR)	0.089 (0.058 – 0.12)	0.19 (0.090 – 0.39)	0.12 (0.070 – 0.17)	0.073 (0.051 – 0.099)
Median V <sub>b</sub> [mL mL <sup>-1</sup> ] (IQR)	0.089 (0.057 – 0.14)	0.036 (0.00063 – 0.086)	0.071 (0.037 – 0.11)	0.095 (0.056 – 0.15)

95%-CI: 95% confidence interval; IQR: interquartile range; MR<sub>glc</sub>: mean glucose metabolic rate computed assuming a lumped constant of 1 and a blood volume fraction of 0; SUV: standardized uptake value with bodyweight correction measured 40 – 50 minutes post injection; K<sub>1</sub>-k<sub>3</sub>: rate constants of the 2-tissue compartment model of glucose metabolism; V<sub>b</sub>: blood volume fraction; VOI: volume of interest. \*one voxel equals a volume 39.75 mm<sup>3</sup>. †calculated after log<sub>e</sub>-transformation.

**Table 4:** Correlation of  $VOI_{\text{tumor}}$  parameters.

	$MR_{\text{glc}}$ and $K_1$	$MR_{\text{glc}}$ and $k_2$	$MR_{\text{glc}}$ and $k_3$	$MR_{\text{glc}}$ and $V_b$	$k_3$ and $V_b$
All lesions (n=104)	0.286 (0.003)*	-0.088 (0.372)	0.488 (<0.001)*	0.189 (0.055)	0.045 (0.652)
NSCLC (n=85)	0.255 (0.018)*	-0.114 (0.298)	0.507 (<0.001)*	0.141 (0.198)	0.102 (0.352)
CRC (n=17)	0.235 (0.363)	-0.039 (0.881)	0.363 (0.152)	0.365 (0.149)	-0.159 (0.541)

Correlations are obtained on a whole-lesion basis, and are expressed as Spearman's  $\rho$  with statistical significance between parentheses.\*statistically significant

**Table 5:** Comparisons between tumor segments.

	$K_1$	$k_2$	$k_3$	$V_b$
All lesions (n=104)	28.1 (< 0.001) Follows Ttrend in 42.3%	26.8 (<0.001) Trend in 40.4%	120.5 (<0.001) Trend in 78.8%	71.6 (<0.001) Trend in 93.3%
NSCLC (n=85)	26.6 (<0.001) Trend in 40.0%	16.3 (<0.001) Trend in 36.5%	99.7 (<0.001) Trend in 77.6%	54.5 (<0.001) Trend in 92.9%
CRC (n=17)	2.5 (0.312) Trend in 47.1%	12.1 (0.002) Trend in 52.9%	17.3 (<0.001) Trend in 82.4%	22.2 (<0.001) Trend in 100%
Plausible † (n=45)	9.0 (0.011) Trend in 40.0%	2.8 (0.247) Trend in 33.3%	37.9 (<0.001) Trend in 68.9%	14.4 (0.001) Trend in 86.7%
Volume >14.1 cm <sup>3</sup> (n=40)	25.6 (<0.001) Trend in 62.5%	43.6 (<0.001) Trend in 65.0%	61.4 (<0.001) Trend in 92.5%	52.9 (<0.001) Trend in 95%

Comparison between tumor segments is expressed as Friedman's  $\chi^2$  with statistical significance between parentheses. A trend between the segments is expressed as a percentage of lesions, for  $K_1 - k_3$  this trend is  $VOI_{high} > VOI_{medium} > VOI_{low}$ , for  $V_b$  this trend is  $VOI_{high} < VOI_{medium} < VOI_{low}$ . † Lesions with all 12 parameters within the defined range of biological plausibility.

Fig. 2

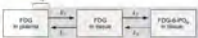


Fig. 3

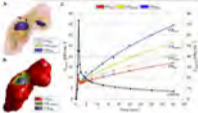


Fig. 4

